# High-throughput space-time Fourier ptychography for motile microorganisms

MING SUN,[†] KAIZHANG KANG,[†] YOGESHWAR NATH MISHRA, XINGE YANG, HADI AMATA, AND WOLFGANG HEIDRICH[*]

*King Abdullah University of Science and Technology (KAUST), Thuwal 23955-6900, Saudi Arabia*
[†]The authors contributed equally to this work.
[*]wolfgang.heidrich@kaust.edu.sa

**Abstract:** High-fidelity imaging of live microorganisms is essential for understanding dynamic biological processes but remains limited by motion blur and insufficient temporal resolution. We present a space-time Fourier ptychography (ST-FP) system optimized for high-throughput, time-resolved quantitative phase imaging of fast-evolving biological specimens. To overcome photon budget and timing constraints, we develop a custom shift-register-based LED panel that enables direct, flicker-free control of illumination patterns, achieving a ~1100× increase in effective irradiance over normal LED panels. This allows for stable imaging at exposure times as short as 800 μs. On the computational side, we formulate an auto-differentiable complex-valued reconstruction framework with GPU acceleration for the object set solution. Our temporal regularization can improve consistency and robustness under complex motion with different illumination conditions. The computational pipeline achieves a ~23× speedup, reducing reconstruction time for a $120 \times 1200 \times 1200$ sequence from 13.7 to 0.59 hours (CPU vs. GPU). We first evaluate our optimized ST-FP through simulations of swirling motion patterns. Then, in a real experiment with a translation motion condition, a ~45× improvement in space-bandwidth-time product (SBP-T) over our prior ST-FP implementation is quantitatively demonstrated using a binary phase target. We further validate the system on grayscale phase samples. We finally test our system for live imaging of vinegar eels and brine shrimp with uncontrolled motion at up to 260 Hz, demonstrating its capability to push the dynamic upper limits of high-throughput Fourier ptychography. The motion-aware reconstruction further enables trajectory tracking and flow field analysis of dynamic biological behaviors.

## 1. Introduction

Studying live microorganisms is essential for understanding biological processes, environmental interactions, and physiological dynamics. Semi-transparent aquatic species such as tardigrades, rotifers, nematodes, and hydra serve as powerful model organisms due to their responsiveness to environmental cues. Tardigrades have been imaged in hydrated conditions to reveal internal structures [1] and studied for species-specific hypoxia resilience [2]. Rotifers have demonstrated both structural defense and active roles in microplastic fragmentation [3,4]. Imaging techniques have also uncovered coordinated neural control of behavior in hydra through gap-junction-mediated contraction [5]. In nematodes like *C. elegans*, high-speed imaging has revealed neuronal activation pathways and motor dynamics [6–8], while collective oscillations in *Turbatrix aceti* swarms have also been visualized [9]. In vertebrate systems, live imaging in zebrafish has enabled visualization of astrocyte morphogenesis [10], and in human stem-cell-derived cardiomyocytes has facilitated functional analysis of calcium signaling [11]. Recent techniques have also enabled four-dimensional, label-free imaging of freely swimming sperm cells [12], as well as classification of sperm under stress using deep learning [13]. The high amount and density of sperm and their rapid movement (up to 180 μm/*s*) require microscopy systems with both a large field of view and high spatial-temporal resolution to enable accurate trajectory tracking.

This challenge is currently circumvented by manually switching between objectives of different magnifications [14]. In environmental applications, identifying diatom genera and assessing cell viability through fluorescence microscopy has proven invaluable [15]. Simultaneously analyzing tens of thousands of such live diatom cells over a large area without compromising spatial and temporal resolution is essential in related research [16]. Likewise, research on immune-cell dynamics involving platelets presents similar challenges for microscopy, as platelets are only about 2 μm in size, activate within milliseconds, and are not amenable to genetic manipulation [17]. These studies illustrate the growing need for microscopy systems that can resolve dynamic biological events with high spatial and temporal fidelity [8,18,19], supporting next-generation live cell imaging.

Despite the availability of high-resolution imaging methods, optical microscopy remains a cornerstone in biological research due to its ability to non-invasively observe live specimens. Among these, quantitative phase imaging (QPI) stands out for visualizing transparent biological samples with high sensitivity and without labeling [20,21]. This label-free nature eliminates complex sample preparation and avoids fluorophore-related limitations such as dye penetration and autofluorescence, making it ideal for imaging of live cells and microorganisms in their native states [22]. Unlike fluorescence-based methods, which often suffer from issues like limited dye penetration, autofluorescence, and photobleaching [23], QPI offers label-free, low-toxicity imaging [24–26]. Traditional label-free modalities such as bright-field and differential interference contrast microscopy offer limited contrast or optical sectioning capability [8,27], whereas QPI enables clear visualization of subcellular features and dynamic processes, offering an invaluable tool for studying structural organization and behavior in live samples. To fully leverage QPI for high-resolution, large-scale, and dynamic imaging, computational imaging techniques have emerged as powerful and scalable solutions.

Fourier ptychography (FP) represents a rapidly advancing QPI system, combining high spatial resolution and large field of view (FOV) through the fusion of multiple low-resolution intensity measurements acquired under angularly varied illuminations [28–30]. By operating with low numerical aperture (NA) objectives, FP enables wide-FOV imaging while computationally recovering high-frequency content in Fourier space. This capability has significantly extended the utility of QPI to large-scale biological samples, such as live cells, tissue cultures, and microorganisms [31,32]. However, conventional FP systems often rely on sequential LED illuminations, resulting in long acquisition times that limit their applicability for fast-moving or dynamic specimens. Recent efforts to accelerate FP have explored multiplexed illumination [33–35]. Building on the advances, we recently proposed a space-time Fourier ptychography (ST-FP) system [36], which integrates compressive sensing with temporal motion priors to jointly reconstruct amplitude, phase, and motion fields. ST-FP demonstrated superior robustness in reconstructing complex live scenes with dynamic morphological changes.

In this work, we proposed a high-speed ST-FP system, enabling effective high-throughput imaging of fast-moving biological specimens. A central challenge in such acquisition is ensuring sufficient photon flux during short exposures. Conventional LED panels, typically configured in a matrix architecture with shared row and column pins, use dynamic refreshing to sequentially illuminate subsets of LEDs. This approach reduces the effective brightness and introduces flickering artifacts when the camera exposure time falls below the refresh period, limiting its use in high-speed imaging. To overcome this, we design a custom LED panel with direct-addressing architecture based on shift-register control, allowing simultaneous activation of arbitrary LED patterns. Our customized LED module also gets ~1100× higher in irradiance compared to a standard LED board. This enables stable, flicker-free illumination for high-frame-rate ST-FP system. On the algorithmic side, we solve the object reconstruction problem in ST-FP within an auto-differentiable optimization framework and accelerate computation using GPUs. Temporal regularization [37–39] enforces consistency across frames, preserving dynamic structures under

changing illumination. Together, these improvements elevate the temporal resolution, robustness, and scalability of ST-FP, making it a powerful tool for high-speed phase imaging of dynamic biological phenomena.

We validate the effectiveness of our system through simulations and experiments. We first analyze the limitations of conventional LED panels, showing how scanning modes and pulse-width modulation (PWM) based brightness control reduce effective brightness and introduce flickering artifacts under short exposure times. Simulations of swirling motion show that low-fps acquisition causes motion blur and degraded phase reconstructions, while our high-fps ST-FP model preserves motion fidelity and improves quality. These findings are further validated experimentally using controlled translations of both binary phase targets and grayscale phase targets. Compared to our recent ST-FP implementation [36], the enhanced system achieves approximately a ~45-fold increase in the space-bandwidth-time product (SBP-T), reflecting substantial enhanced throughput. We further demonstrate high-speed live imaging of microorganisms, including brine shrimp and vinegar eels, at up to 260 fps with 800 μs exposure times. Across all scenarios, shorter exposures and higher frame rates yield sharper, more temporally consistent reconstructions. Finally, the dense temporal sampling also enables robust velocity field estimation and point trajectory tracking, offering motion coordination and behavioral dynamics. Our results establish the high-throughput ST-FP platform as a versatile tool for time-resolved QPI of live, rapidly evolving biological systems.

## 2. Methodology

### 2.1. Space-time Fourier ptychography

Here we first give an overview of Fourier ptychography (FP). The hardware typically consists of an LED matrix and a normal research microscope, as shown in Fig. 1(b). Each LED with index $m$ results in a (spatially coherent) plane wave at the object $\mathbf{o}$, with the specific angle of illumination corresponding to the spatial frequency $\mathbf{k}_m = (k_{xm}, k_{ym})$. This process corresponds to a shift in the Fourier domain controlled by the angle of illumination, and then filtered by the pupil function $\mathbf{H}$ [29,30]. This resulting spectrum is then inverse Fourier transformed to form the intensity at the sensor plane:

$$\mathbf{I}_m(\mathbf{o}(\mathbf{r})) = \left| \mathcal{F}^{-1}[\mathcal{F}[\mathbf{o}(\mathbf{r})\exp(j\mathbf{k}_m\cdot\mathbf{r})]\mathbf{H}(\mathbf{k})] \right|^2 , \tag{1}$$

where $\mathcal{F}$ and $\mathcal{F}^{-1}$ respectively represent the 2D Fourier transform and its inverse, and $j$ is the imaginary unit. $\mathbf{r} = (x, y)$ and $\mathbf{k} = (k_x, k_y)$ denote the coordinates at the spatial and frequency plane, respectively. For simplicity, we will use the notation $\mathbf{I}_m(\mathbf{o})$ in the following text, neglecting the explicit dependence on the spatial coordinate $\mathbf{r}$.

Long acquisition times limit the ability to image moving live samples using FP. Our recent work space-time Fourier ptychography (ST-FP) [36] utilizes multiplexed illumination scheme [33,40,41] to mitigate this problem by simultaneously activating multiple LEDs according to binary activation patterns $\mathbf{P}_t$. The measured image at time $t$ follows the formation model:

$$\mathcal{A}_t(\mathbf{o}) = \sum_{m=1}^{N_{LED}} \mathbf{P}_{t,m}\mathbf{I}_m(\mathbf{o}), \tag{2}$$

where $\mathbf{P}_{t,m} \in \{0, 1\}$ denotes the activation state of the LED with index $m$ at time $t$. To maintain consistent illumination intensity across frames, LEDs are grouped based on their illumination angles, and each pattern vector $\mathbf{P}_t$ is designed to activate a similar number of LEDs within each group.

ST-FP can reconstruct a *time-varying* object $\mathbf{o}_t$, which has a different, deformed geometry at every time $t$. The objective of ST-FP is to leverage temporal information to extract additional
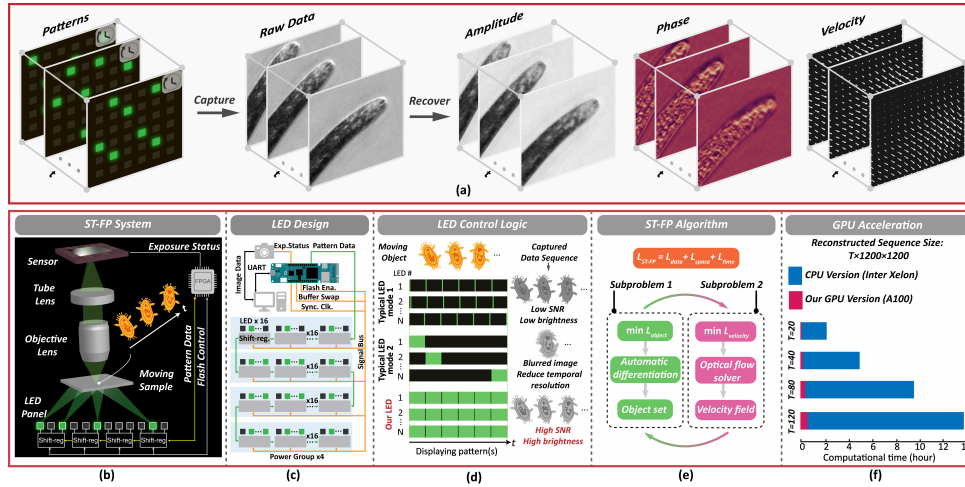
**Fig. 1.** Overview of the high-performance ST-FP system. (a) By leveraging our fast and stable illumination hardware, ST-FP captures high-speed raw data and reconstructs high-fidelity amplitude, phase, and velocity fields. (b) Schematic of the ST-FP system, based on a shift-register-controlled LED panel for fast and stable illumination. (c) LED module design using an array of shift-register LED drivers. This configuration allows the system to simultaneously illuminate all LEDs based on preloaded data, which maximizes the effective brightness of each LED. (d) Comparison of LED control logics under multiplexed illumination. Conventional sequential refreshing with short exposures, causing serious noise. Sequential refreshing with long exposures (low fps) leads to motion blur and reduced temporal resolution. Our static shift-register control (high fps) enables high-contrast, high-SNR imaging without flicker. (e) ST-FP reconstruction framework: the optimization problem is split into object and flow subproblems, solved alternately using automatic differentiation and optical flow solvers. (f) GPU acceleration results: compared to the old implementation [36], our GPU-accelerated version dramatically reduces computational time for long-sequence reconstructions.

motion information, thereby increasing the SBP-T of the reconstruction and enabling imaging of dynamic states of the object across different frames. As a side benefit, ST-FP also provides an estimate of the object motion $\mathbf{v}_t$ over time. Specifically, ST-FP exploits the inherent temporal coherence between contiguous frames to refine the joint estimation of object and motion. We formulate an optimization problem that concurrently considers neighboring frames, thereby enforcing consistency in the motion estimation process across the temporal dimension. By integrating this strategy, we effectively close the numerical reconstruction loop, ensuring that the reconstructed motion information closely aligns with the actual dynamics present within the scene. Overall, the joint optimization framework of ST-FP can be described as:

$$\min_{\{\mathbf{o}_t, \mathbf{v}_t\}_t} \quad \mathcal{L}_{\text{data}} + \mathcal{L}_{\text{space}} + \mathcal{L}_{\text{time}}, \tag{3}$$

where $\mathcal{L}_{\text{data}}$ represents the data fidelity loss based on the measured multiplexed images, $\mathcal{L}_{\text{space}}$ includes spatial regularization terms on the object and motion fields, and $\mathcal{L}_{\text{time}}$ includes temporal consistency regularization across frames. More details are provided in Supplement 1, S1.

## 2.2. High-performance ST-FP system

The original ST-FP framework [36] demonstrated dynamic QPI capabilities. However, its practical performance for high-speed imaging of live biological samples was fundamentally constrained

by the use of standard commercial LED panels. These panels employed a matrix-addressing and dynamic refreshing scheme, in which only a fraction of LEDs were illuminated at any given time. It significantly reduced the effective brightness, necessitating longer exposure times (87 ms in the original ST-FP [36]) and introducing flickering artifacts under short-exposure conditions, thereby degrading image quality. In addition, the limited brightness of typical LEDs compromised the achievable signal-to-noise ratio (SNR), which makes it hard to achieve high-fidelity phase recovery at high frame rates. Computational efficiency was also a limitation: the original ST-FP reconstruction took approximately one hour to process a $20 \times 1200 \times 1200$ sequence in limited iterations. A GPU-accelerated implementation and a more efficient solver are therefore necessary for practical reconstruction of long-sequence data. To overcome these limitations, we developed a high-performance ST-FP system incorporating a shift-register-based LED module, a high-frame-rate camera, and an optimized GPU-accelerated reconstruction algorithm. This system maximizes the photon budget per exposure, eliminates flickering artifacts, and significantly enhances the dynamic imaging capability of ST-FP.

Low frame rate (frames per second, fps) acquisition using the multiplexed illumination patterns yields longer exposure time, and the raw data captured after passing through the FP system suffer from temporal integration effects, resulting in blurred features. In Fig. 1(a), our high-fps ST-FP system mitigates these issues by enabling much shorter exposure times, made possible by the higher brightness of our newly designed LED panel. The raw data captured is of higher contrast and preserves fine structural details with minimal motion blur. This improvement in raw data quality leads to significantly enhanced ST-FP reconstructions, as evidenced by the sharper and more accurate amplitude, phase, and motion field results.

Specifically, to enable high-speed imaging, we redesigned the illumination system by developing an LED matrix and optimizing the LED control logic, as illustrated in Figs. 1(b)-(d). The key insight is that maximizing the number of photons received per unit time–referred to as effective brightness–is critical for achieving shorter exposure times and higher frame rates. However, traditional LED panels introduce significant bottlenecks: they employ a matrix-addressing scheme with dynamic refreshing, where only subsets of LEDs are illuminated sequentially. This approach substantially reduces the effective brightness and causes flickering artifacts when the sensor's exposure time is shorter than the refreshing cycle, limiting the applicability for high-speed ST-FP. To overcome this limitation, our LED module is driven by an array of shift-register circuits, with each LED independently controlled by a dedicated pin, as shown in Figs. 1(b)-(c). This architecture eliminates the need for dynamic refreshing, allowing simultaneous illumination of all selected LEDs based on preloaded pattern data, thereby maximizing the effective brightness. Our LED module is at least ~1100× higher in irradiance compared to a standard off-the-shelf LED board (see Supplement 1, S2). Furthermore, the shift-register design incorporates a double-buffering mechanism, enabling new patterns to be loaded while maintaining continuous illumination, so that the maximum achievable frame rate is constrained only by data transfer speed. The design logic of our LED module is shown in Fig. 1(c). To further enhance imaging quality, we selected high-efficiency green LEDs with a narrow 5 nm spectral bandwidth, maximizing the signal-to-noise ratio (SNR) while minimizing chromatic aberrations. Combined with a high-frame-rate camera and illumination multiplexing strategies, this hardware setup enables reliable, high-speed acquisition. In Fig. 1(d), we compare different LED control logics under multiplexed illumination modes. In conventional LED panels, LEDs are illuminated sequentially, meaning that achieving higher illumination rates comes at the cost of shorter effective exposure times, leading to significant fluctuations and increased risk of desynchronization between the LED control and the camera trigger–an unreliable solution for practical high-speed imaging. Alternatively, using longer exposure times to accommodate the refreshing cycles (low-fps case) reduces temporal resolution and leads to blurred image capture. In contrast, our shift-register-based LED design simultaneously controls all LEDs in real time (high-fps case), producing

high-brightness, high-SNR images without introducing flicker or timing mismatch. This static, simultaneous scanning approach offers superior stability, minimizes brightness loss, and ensures reliable, high-quality data capture for high-speed ST-FP imaging. More detailed analysis of the limitations of conventional LED panels, including scanning mode and pulse-width modulation (PWM) control is provided in the Supplement 1, S3.

Beyond hardware improvements, we also optimized the ST-FP reconstruction algorithm to achieve faster and more robust recovery, as shown in Figs. 1(e)-(f). In Fig. 1(e), ST-FP objective function combines a data fidelity term with spatial and temporal regularization terms. To facilitate efficient optimization, we split the overall problem into two subproblems: one for the complex-valued object set and the other for the motion (flow) field set. These two subproblems are updated alternately. Compared to the original ST-FP framework, some algorithmic improvements have been introduced. We transition from solving the object subproblem via ADMM to an automatic differentiation-based approach [42]. Specifically, after passing through the forward model and loss function, gradients are computed and back propagated to optimize the object set using Adam optimization [43]. In addition, the entire framework has been migrated to a GPU-accelerated version. As shown in Fig. 1(f), the GPU implementation results in a substantial reduction in computational time compared to the original CPU-based solver, enabling practical reconstruction of long, high-resolution sequences. Furthermore, since ST-FP reconstruction involves optimizing a long temporal sequence, we implement a recurrent processing scheme that reduces computational complexity and peak memory usage, thereby improving overall computational efficiency (see Supplement 1, S5). Together, these hardware and algorithmic enhancements enable high-speed ST-FP imaging with practical throughput and robustness.

## 3.  Results

### 3.1.  Simulation

In the simulation, the illumination wavelength is set to 530 nm. The sensor has a pixel size of 3 μm, and the microscope system uses a 5× objective lens. The objective lens has a numerical aperture of $NA_{\text{obj}} = 0.14$. The LED array consists of $14 \times 14$ elements, with an adjacent gap of 4 mm and a vertical distance of 80 mm from the sample. To simulate objects undergoing non-rigid motion, we generated a swirling motion by applying a 2D swirl transformation to the complex-valued object across frames. The swirl strength varied cyclically across 120 frames using a piecewise linear profile: first increasing from −0.5 to 0.5 over 40 frames, then decreasing from 0.5 to −0.5 over the next 40 frames, and finally increasing again from −0.5 to 0.5 over the subsequent 40 frames. This pattern created a repeated swirl motion with direction reversals, simulating dynamic rotational deformation in a temporally structured manner. To emulate low frame rate acquisition (acquired at 1/10 the frame rate of the high-fps case) under multiplexed illumination, raw low-fps data were generated by summing sequential measurements corresponding to repeated illumination patterns, integrating over multiple motion states within each low-fps exposure. In contrast, high-fps data preserved individual illumination patterns at each time step, enabling finer temporal resolution.

Figure 2(a) shows reconstructions from ST-FP at low fps, high fps (ours), and ground truth (GT) for selected frames. Insets in the lower right corners of the amplitude panels show the corresponding raw data for low-fps and high-fps cases. Figure 2(b) illustrates the phase results and the GT corresponding to Fig. 2(a). To enable a direct frame-by-frame comparison with the high-fps case, we temporally upsampled the low-fps sequence by duplicating each frame ten times. This process produced a quasi-output matching the temporal resolution of the high-fps sequence, facilitating a direct comparison. Note that in the following comparisons, we adopt the same strategy to upsample the low-fps sequences by the corresponding temporal fold factor. Figure 2(c) summarizes quantitative metrics, including the structural similarity index (SSIM), which measures perceptual similarity, and the mean squared error (MSE), which quantifies

pixel-wise reconstruction error, for amplitude and phase reconstructions across all frames, comparing the low-fps and high-fps results. In the low-fps case, each frame integrates motion over a prolonged period, leading to blur and loss of fine spatial details. This blurring effect is particularly visible in the finer structures of the resolution target, where overlapping motion creates artifacts that distort the spatial features. In contrast, the high-fps case preserves individual motion steps, maintaining sharper and more distinguishable structures. This enhances space-time optimization, leading to more stable and higher-quality amplitude and phase reconstructions.
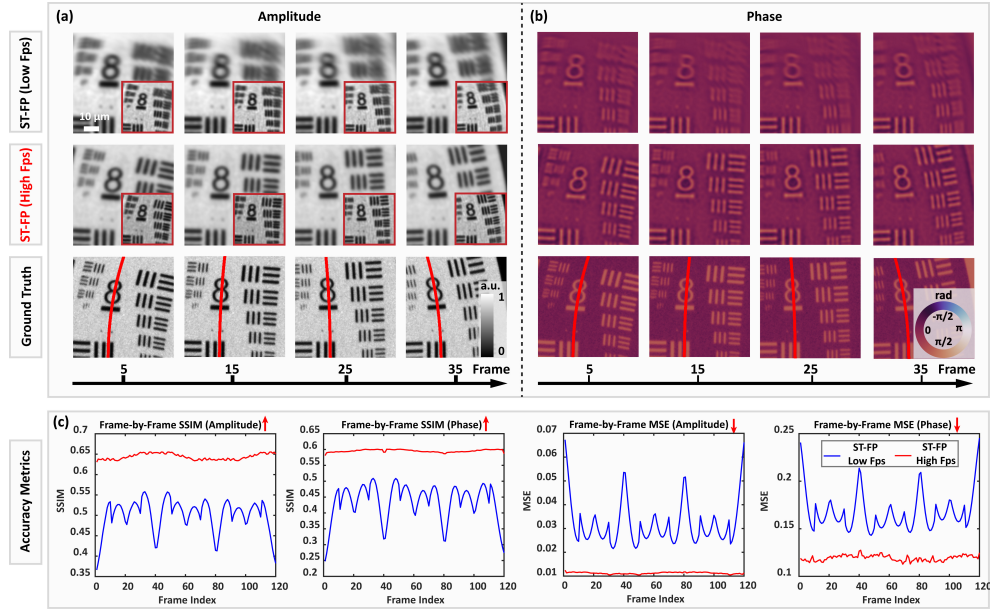


**Fig. 2.** Comparison of ST-FP reconstructions under different frame rates with simulated swirl motion (see Visualization 1). (a) Amplitude reconstructions from ST-FP at low fps, high fps (ours), and ground truth for selected frames. Insets in the lower right corners of the amplitude panels show the corresponding raw data for low-fps and high-fps cases. (b) Phase reconstructions from ST-FP at low fps, high fps, and ground truth for selected frames. (c) Accuracy metrics, including SSIM and MSE for amplitude and phase reconstructions across frames, comparing low-fps and high-fps results.

### 3.2. Experiments of moving target (binary and gray scale samples)

In our experimental setup, the dominant illumination wavelength of LED is 524 nm. Light transmitted through the sample is collected by a 5× objective lens (Mitutoyo M Plan Apo, 0.14 NA), relayed via a tube lens (Thorlabs TTL200-S8) to a LUCID Atlas10 camera (ATX081S-MC, 8.1 MP, 2.74 μm pixel size). Our LED array consists of 14×14 LEDs, with a gap of 4 mm between adjacent LEDs and a vertical distance of ~80 mm from the sample. To ensure high-bandwidth data transmission, we use a 10G PoE++ switch to meet both the power and data rate requirements of the camera. We deploy an EB-LINK Intel X550-T2 10G Ethernet adapter, which enables the system to utilize the camera's high frame rate capabilities.

To evaluate the impact of frame rate on imaging moving objects, we conducted an experiment using a USAF phase target mounted on a translation stage. The target was manually translated along a single direction, and data was captured under two different frame rate conditions: low frame rate (20 Hz, 20 ms exposure time) and high frame rate (260 Hz, 1 ms exposure time). Figure 3(a) shows the raw intensity image of the static USAF phase target captured under

single-LED illumination. A zoomed-in region of interest (ROI) is highlighted in Fig. 3(b). Figure 3(c) presents the corresponding phase reconstruction from traditional FP under static conditions as a reference. Figure 3(d) shows the raw data captured at low fps, where the long exposure time causes motion blur, particularly visible in the finer structures of the target. As a result, the reconstructed phase in Fig. 3(e) suffers from severe blurring, making it challenging to retrieve high-frequency details. In contrast, our high-fps capture in Fig. 3(f) significantly reduces motion blur by preserving individual motion steps with minimal distortion. The observed differences in raw data quality directly impact the performance of ST-FP, providing a temporally consistent dataset, allowing the ST-FP algorithm to accurately reconstruct fine details with improved contrast and reduced artifacts, as shown in Fig. 3(g).
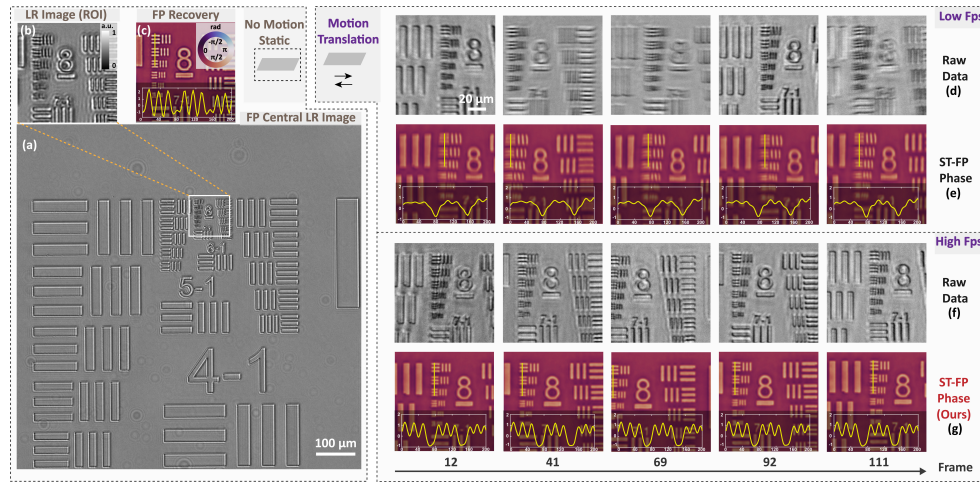


**Fig. 3.** Comparison of ST-FP under different frame rate conditions using a moving phase target (see Visualization 2). (a) Raw intensity image of USAF phase target from a single central LED under the static condition. (b) Zoomed-in region of interest (ROI) from (a). (c) Reference phase reconstruction from traditional FP. (d) Raw intensity images acquired at low fps. (e) Phase reconstructions from ST-FP using the low-fps dataset in (d). (f) Raw intensity images acquired at high fps. (g) Phase reconstructions from ST-FP using the high-fps dataset in (f).

To quantitatively assess the system's imaging performance, we calculated the space-bandwidth product (SBP) and space-bandwidth-time product (SBP-T) based on the optical parameters and acquisition speed. The effective FOV in the object plane was measured to be 876.8 μm × 876.8 μm, with a full-pitch resolution of approximately 1.56 μm. This corresponds to 562 × 562 resolvable spots across the width and height, yielding an SBP of 0.3159 megapixels. Given the high-speed acquisition at 260 fps, the corresponding SBP-T reaches ~82.1 megapixels per second. Compared to our original ST-FP system [36] operating at 1.82 megapixels per second, the improved system achieves a ~45-fold increase in SBP-T. This significant enhancement in SBP-T directly translates to improved imaging throughput, enabling high-resolution dynamic imaging over a large FOV with substantially reduced acquisition time.

To clarify the resolution design and performance of our system, we considered three reference cases. Under single-LED central illumination, the resolution is approximately 3.74 μm, corresponding to an effective NA of 0.14. With our multiplexed illumination pattern with a dominant illumination NA of ~0.24, the synthetic NA increases to ~0.38, yielding a theoretical resolution around 1.37 μm [44]. Experimentally, we achieve a full-pitch resolution of approximately 1.56 μm. These results confirm that the system delivers a ~2.73× resolution enhancement over the

single-LED case. The measured resolution aligns well with design expectations, considering practical factors such as motion blur, noise, and partial coherence. In addition to binary targets such as the USAF resolution target, we also evaluated another grayscale phase target under controlled motion conditions (see Visualization 3 and Supplement 1, S4).

### 3.3. Experiments on live microorganisms

To evaluate the performance of our ST-FP method, we also compare it against conventional CS-FP, a state-of-the-art technique that enables accelerated FP imaging by using multiplexed illumination and compressed sensing principles (see more details in [36,41]). While CS-FP assumes the sample remains quasi-static over the acquisition of a few illumination patterns, this assumption often breaks down in dynamic scenes, leading to artifacts and degraded reconstructions. ST-FP addresses this limitation by explicitly modeling time-varying objects and integrating motion estimation into the reconstruction process. We validate the effectiveness of ST-FP on real dynamic samples by imaging a freely swimming brine shrimp under two acquisition regimes: a low-frame-rate condition (20 Hz, 20 ms exposure) and a high-frame-rate condition (260 Hz, 0.8 ms exposure). The experimental setup matches that described in Section 3.2.

Since the motion of the live sample is naturally uncontrolled and non-repeatable, it is not possible to reproduce identical movements under both acquisition settings. Instead, we ensured that both sequences captured the same specimen undergoing qualitatively similar dynamic behaviors within a short time window. This allows a fair comparison between the two frame-rate conditions, simulating the imaging of similar motion patterns under differing temporal resolutions.

We tested the system on a freely swimming vinegar eel. Figure 4 shows a comparative evaluation of reconstruction quality. In the low-fps setting, CS-FP results in Figs. 4(a)-(b) exhibit substantial degradation due to motion blur. ST-FP reconstructions in Figs. 4(c)-(d) show partial improvement due to motion-aware modeling. However, the quality of raw measurements remains a limiting factor: strong blur and low SNR make accurate flow estimation difficult, which can in turn lead to suboptimal object recovery. As a result, some reconstructed features may appear inconsistent with the raw frame structures, particularly in rapidly moving regions.
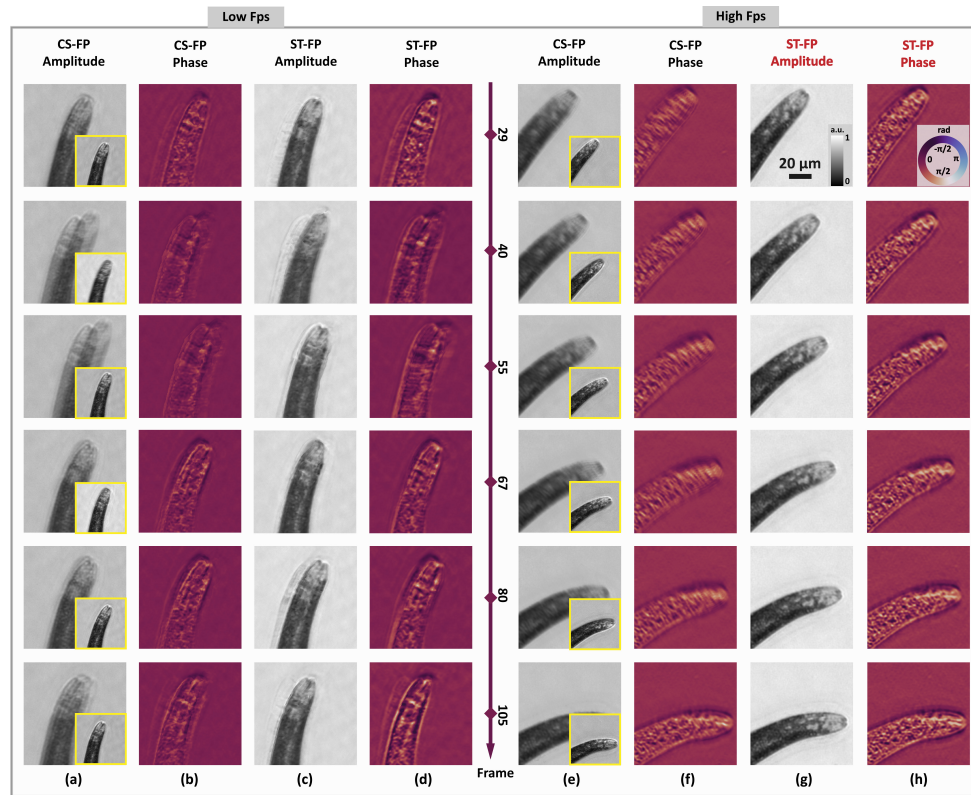
Under high-fps conditions, CS-FP reconstructions in Figs. 4(e)-(f) improve as motion blur is reduced, but dynamic inconsistencies and jitter persist due to the static-scene assumption during sequential illumination. In contrast, ST-FP in Figs. 4(g)-(h) yields the highest fidelity. The amplitude reconstructions show well-defined edges, and the phase maps capture fine structural variations and continuous motion-induced deformations with minimal artifacts.

### 3.4. Trajectory tracking and velocity field visualization

Beyond improving reconstruction fidelity in dynamic conditions, our ST-FP framework also enables velocity field estimation and motion tracking. In Fig. 5, we demonstrate this motion-aware capability using a swimming vinegar eel. Figure 5(a) compares representative frames from four cases–low-fps CS-FP, low-fps ST-FP, high-fps CS-FP, and our high-fps ST-FP–highlighting clear differences in motion tracking quality. Our high-fps ST-FP achieves the most accurate and consistent tracking, as evidenced by the yellow center points, corresponding optical flow fields, and seed point trajectories. See more details in Visualization 5. Figure 5(b) shows high-fps ST-FP results at three representative time points, where yellow lines link the same tracked points across frames, capturing smooth and biologically relevant motion patterns. These results illustrate that our novel ST-FP functions as a robust framework for dynamic motion analysis. We further include one additional example of a brine shrimp (see Supplement 1, S4 Visualization 6, and Visualization 7).

To further showcase the tracking of structurally meaningful features, we analyzed a third dataset involving a specimen exhibiting a stretching-type deformation (150 fps), as shown in Fig. 6. The tracked region corresponds to the end part of a prominent dark structure, serving as a
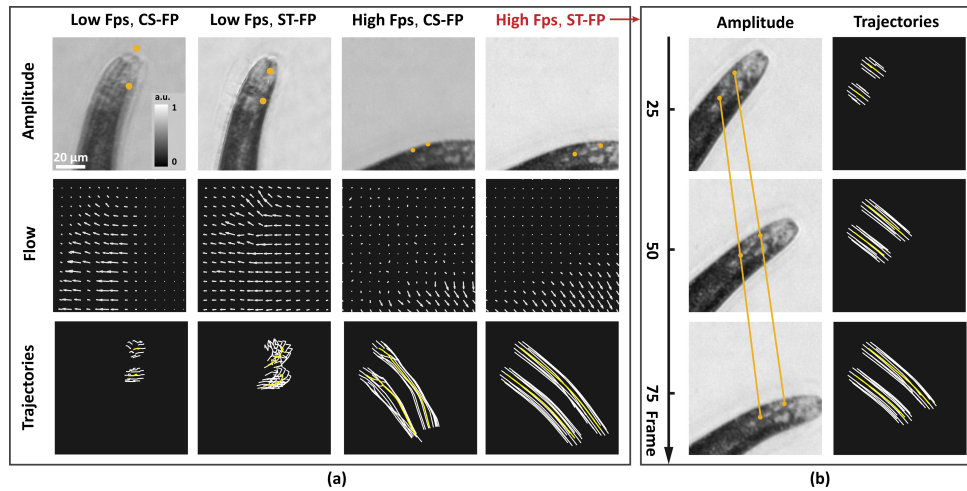
**Fig. 4.** Comparison of CS-FP and ST-FP reconstructions for a dynamically swimming vinegar eel under low and high frame rate conditions. (a)-(b) Amplitude and phase reconstructions using conventional CS-FP at low fps. (c)-(d) Corresponding amplitude and phase reconstructions using ST-FP at low fps. (e)-(f) Amplitude and phase results of CS-FP at high fps. (g)-(h) Corresponding results of ST-FP at high fps. Insets in (a) and (e) display the raw intensity frames. Frame indices mark selected time points across the sequence. High-speed ST-FP enables sharper reconstructions and reduced motion artifacts across dynamic regions (see Visualization 4).

biologically relevant landmark. The amplitude reconstructions in Fig. 6(a) retain sharp structural detail throughout the motion sequence. Figure 6(b) shows 2D optical flow fields. The trajectories of all seed points in Fig. 6(c), with the yellow line marking the motion of the tracked center, quantify the temporal evolution of the deformation axis. ST-FP enables high-fidelity analysis of non-rigid, biologically meaningful dynamics.

## 4. Conclusion and discussion

In this work, we presented a high-performance space-time Fourier ptychography (ST-FP) system designed to enable high-throughput quantitative phase imaging of live, dynamic biological specimens. By addressing key limitations of conventional FP–such as motion blur, limited photon budget, and slow acquisition- our system integrates innovations in both hardware and computation. On the hardware side, our new shift-register-based LED panel enables direct, flicker-free control of illumination patterns, achieving up to a ~1100× increase in effective irradiance compared to a commercial normal LED panel. This supports stable imaging at exposure times as short as 800 μs and frame rates up to 260 fps. On the computational side, we developed a GPU-accelerated,

**Fig. 5.** Motion visualization of a swimming vinegar eel (see Visualization 5). (a) Comparison of low-fps CS-FP, low-fps ST-FP, high-fps CS-FP, and high-fps ST-FP (ours) reconstructions. This representative frame from each case highlights the differences in motion tracking quality, with our high-fps ST-FP achieving the most accurate and consistent tracking. Amplitude reconstructions (top) show yellow points marking the center of tracked elliptical seed point clouds; middle row shows corresponding 2D optical flow fields; bottom row shows trajectories of all seed points (10 points each). (b) High-fps ST-FP results at three representative time points, with amplitude images (left) and trajectories (right), where yellow lines link the same tracked points across frames.

auto-differentiable reconstruction framework with temporal regularization, reducing computation time by up to 23× while enabling accurate recovery of high-resolution sequences (e.g., 120 × 1200 × 1200). Comprehensive simulations and experiments confirm significant improvements in temporal fidelity, motion robustness, and throughput. In particular, we demonstrate a ~45× increase in space-bandwidth-time product (SBP-T) and superior reconstruction quality in both controlled and live microorganism imaging. To ensure sample safety under such high illumination power, we empirically optimized the exposure duration to balance between sufficient signal and thermal effects. In our experiments, we observed little photothermal damage to live specimens. The reduced exposure time not only mitigates heating but also minimizes motion blur, enabling high-fidelity capture of fast biological dynamics. A more systematic thermal characterization across diverse samples remains an important direction for future studies. Our results underscore the power of hardware-software co-design in advancing dynamic FP phase imaging.

It is worth noting that our framework operates under several assumptions. It relies on moderate temporal coherence and structural continuity to enable warping-based modeling, as typically observed in semi-rigid or smoothly deforming samples like microorganisms or tissues. In contrast, scenes with sparse and fast-moving particles with uncorrelated motion [45] may lead to artifacts or loss of transient structures. The method also assumes passive samples without self-emission, such as non-bioluminescent organisms–an inherent constraint of FP, which is not compatible with self-luminous specimens. Addressing these challenges would require motion models that account for discontinuities, sparsity, along with extensions such as spectral unmixing, time-resolved detection, or hybrid modeling of illumination and emission processes [46,47]. Finally, the motion-resolved capability of ST-FP positions it as a potential tool for studying microscale predator-prey interactions in microbial ecosystems [48], embryonic development in live animal models [49], and biomechanical stress propagation in living tissues [50]. Future
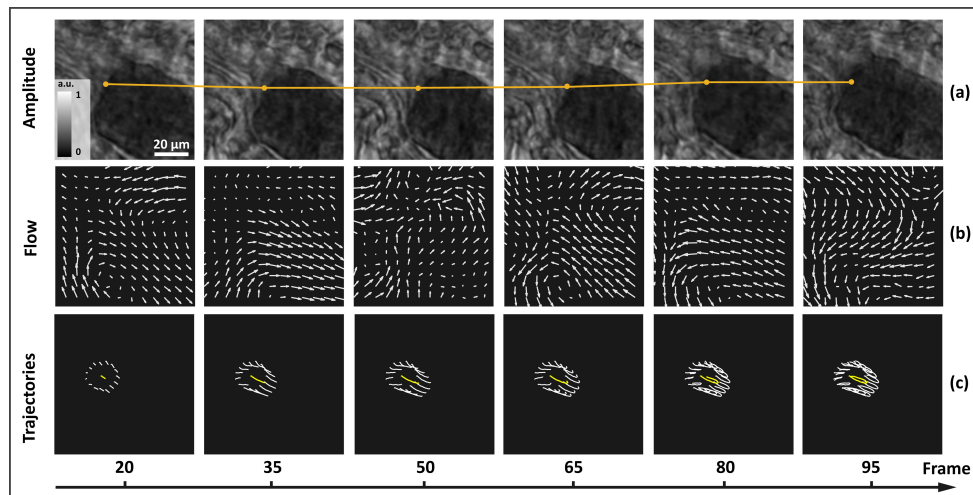
**Fig. 6.** Motion analysis of a stretching-type deformation in a live brine shrimp using high-fps ST-FP (see Visualization 8). (a) Representative amplitude reconstructions from high-fps ST-FP frames, showing continuous morphological changes. Yellow points indicate the center of the tracked elliptical seed point cloud. (b) Corresponding 2D optical flow fields estimated between successive frames. (c) Tracked trajectories of an elliptical seed point cloud (15 points) over time, highlighting the motion evolution of the selected region. The yellow line marks the center trajectory in each frame.

directions include incorporating deep learning-based motion priors and extending the platform to multimodal imaging, such as fluorescence [51–53] or volumetric techniques [54,55], broadening its applications in biology, medicine, and environmental science.

**Disclosures.** The authors declare no conflicts of interest.

**Data availability.** Data underlying the results presented in this paper are not publicly available at this time but may be obtained from the authors upon reasonable request.

**Supplemental document.** See Supplement 1 for supporting content.

## References

1. M.-T. Hong, G. Lee, and Y.-T. Chang, "A non-invasive, label-free method for examining tardigrade anatomy using holotomography," Tomography **11**(3), 34 (2025).
2. P. Hagelbäck and K. I. Jönsson, "An experimental study on tolerance to hypoxia in tardigrades," Front. Physiol. **14**, 1249773 (2023).
3. X. Yin, W. Jin, Y. Zhou, *et al.*, "Hidden defensive morphology in rotifers: Benefits, costs, and fitness consequences," Sci. Rep. **7**(1), 4488 (2017).
4. J. Zhao, R. Lan, W. Zhenyu, *et al.*, "Microplastic fragmentation by rotifers in aquatic ecosystems contributes to global nanoplastic pollution," Nat. Nanotechnol. **19**, 406–414 (2024).
5. Y. Takaku, J. S. Hwang, A. Wolf, *et al.*, "Innexin gap junctions in nerve cells coordinate spontaneous contractile behavior in hydra polyps," Sci. Rep. **4**(1), 3573 (2014).
6. R. Peesapati, B. Austin-Byler, F. Nawaz, *et al.*, "A specific folate activates serotonergic neurons to control c. elegans behavior," Nat. Commun. **15**(1), 8471 (2024).
7. T. Ahamed, A. Costa, and G. Stephens, "Capturing the continuous complexity of behaviour in caenorhabditis elegans," Nat. Phys. **17**(2), 275–283 (2021).
8. S. Rashtchian, K. Youssef, P. Rezai, *et al.*, "High-speed label-free confocal microscopy of caenorhabditis elegans with near infrared spectrally encoded confocal microscopy," Biomed. Opt. Express **12**(6), 3607–3618 (2021).
9. A. Peshkov, S. McGaffigan, and A. C. Quillen, "Synchronized oscillations in swarms of nematode turbatrix aceti," Soft Matter **18**(6), 1174–1182 (2022).
10. J. Chen, K. Poskanzer, M. Freeman, *et al.*, "Live-imaging of astrocyte morphogenesis and function in zebrafish neural circuits," Nat. Neurosci. **23**(1), 1–2 (2020).

11. V. Astro, G. Ramirez-Calderon, R. Pennucci, *et al.*, "Fine-tuned kdm1a alternative splicing regulates human cardiomyogenesis through an enzymatic-independent mechanism," iScience **25**(7), 104665 (2022).
12. G. Dardikman-Yoffe, S. K. Mirsky, I. Barnea, *et al.*, "High-resolution 4-D acquisition of freely swimming human sperm cells without staining," Sci. Adv. **6**(15), eaay7619 (2020).
13. A. Butola, D. Popova, D. Prasad, *et al.*, "High spatially sensitive quantitative phase imaging assisted with deep neural network for classification of human spermatozoa under stressed condition," Sci. Rep. **10**(1), 13118 (2020).
14. C. Dai, Z. Zhang, G. Shan, *et al.*, "Advances in sperm analysis: techniques, discoveries and applications," Nat. Rev. Urol. **18**(8), 447–467 (2021).
15. S. Agustí, J. Krause, I. Marquez, *et al.*, "Arctic (Svalbard islands) active and exported diatom stocks and cell health status," Biogeosciences **17**(1), 35–45 (2020).
16. X. Wu, N. Zhou, Y. Chen, *et al.*, "Lens-free on-chip 3D microscopy based on wavelength-scanning Fourier ptychographic diffraction tomography," Light: Sci. Appl. **13**(1), 237 (2024).
17. S. J. Montague, Y. J. Lim, W. M. Lee, *et al.*, "Imaging platelet processes and function–current and emerging approaches for imaging in vitro and in vivo," Front. Immunol. **11**, 78 (2020).
18. W. Song, A. Matlock, S. Fu, *et al.*, "LED array reflectance microscopy for scattering-based multi-contrast imaging," Opt. Lett. **45**(7), 1647–1650 (2020).
19. C. Védère, L. Vieublé Gonod, N. Nunan, *et al.*, "Opportunities and limits in imaging microorganisms and their activities in soil microhabitats," Soil Biol. Biochem. **174**, 108807 (2022).
20. V. Micó, J. Zheng, J. Garcia, *et al.*, "Resolution enhancement in quantitative phase microscopy," Adv. Opt. Photonics. **11**(1), 135–214 (2019).
21. Y. Park, C. Depeursinge, and G. Popescu, "Quantitative phase imaging in biomedicine," Nat. Photonics **12**(10), 578–589 (2018).
22. T. L. Nguyen, S. Pradeep, R. L. Judson-Torres, *et al.*, "Quantitative phase imaging: recent advances and expanding potential in biomedicine," ACS Nano **16**(8), 11516–11544 (2022).
23. P. Laissue, R. Alghamdi, P. Tomancak, *et al.*, "Assessing phototoxicity in live fluorescence imaging," Nat. Methods **14**(7), 657–661 (2017).
24. M. Chen, Z. F. Phillips, and L. Waller, "Quantitative differential phase contrast (DPC) microscopy with computational aberration correction," Opt. Express **26**(25), 32888–32899 (2018).
25. C. Wang, Q. Fu, X. Dun, *et al.*, "Quantitative phase and intensity microscopy using snapshot white light wavefront sensing," Sci. Rep. **9**(1), 1–12 (2019).
26. H. Lichte and M. Lehmann, "Electron holography-basics and applications," Rep. Prog. Phys. **71**(1), 016102 (2007).
27. S. Coquoz, P. J. Marchand, A. Bouwens, *et al.*, "Label-free three-dimensional imaging of caenorhabditis elegans with visible optical coherence microscopy," PLoS One **12**(7), e0181676 (2017).
28. S. Jiang, P. Song, T. Wang, *et al.*, "Spatial- and Fourier-domain ptychography for high-throughput bio-imaging," Nat. Protoc. **18**(7), 2051–2083 (2023).
29. G. Zheng, R. Horstmeyer, and C. Yang, "Wide-field, high-resolution Fourier ptychographic microscopy," Nat. Photonics **7**(9), 739–745 (2013).
30. G. Zheng, C. Shen, S. Jiang, *et al.*, "Concept, implementations and applications of Fourier ptychography," Nat. Rev. Phys. **3**(3), 207–223 (2021).
31. Y. Shu, J. Sun, J. Lyu, *et al.*, "Adaptive optical quantitative phase imaging based on annular illumination Fourier ptychographic microscopy," PhotoniX **3**(1), 24 (2022).
32. R. Wu, Z. Luo, M. Liu, *et al.*, "Fast Fourier ptychographic quantitative phase microscopy for in vitro label-free imaging," Biomed. Opt. Express **15**(1), 95–113 (2024).
33. L. Tian, Z. Liu, L.-H. Yeh, *et al.*, "Computational illumination for high-speed in vitro Fourier ptychographic microscopy," Optica **2**(10), 904–911 (2015).
34. Y. Xiao, S. Wei, S. Xue, *et al.*, "High-speed Fourier ptychographic microscopy for quantitative phase imaging," Opt. Lett. **46**(19), 4785–4788 (2021).
35. K. Lee, K. C. Lee, J. Jung, *et al.*, "High-resolution display screen as programmable illumination for Fourier ptychography," Opt. Lasers Eng. **177**, 108121 (2024).
36. M. Sun, K. Wang, Y. N. Mishra, *et al.*, "Space-time Fourier ptychography for in vivo quantitative phase imaging," Optica **11**(9), 1250–1260 (2024).
37. G. Zang, R. Idoughi, R. Tao, *et al.*, "Warp-and-project tomography for rapidly deforming objects," ACM Trans. Graph. **38**(4), 1–13 (2019).
38. P. Getreuer, "A survey of gaussian convolution algorithms," Image Process. Line **3**, 286–310 (2013).
39. S. Pollnow, N. Pilia, G. Schwaderlapp, *et al.*, "An adaptive spatio-temporal gaussian filter for processing cardiac optical mapping data," Comput. Biol. Med. **102**, 267–277 (2018).
40. L. Tian, X. Li, K. Ramchandran, *et al.*, "Multiplexed coded illumination for Fourier ptychography with an LED array microscope," Biomed. Opt. Express **5**(7), 2376–2389 (2014).
41. X. Li, L. Li, X. Liu, *et al.*, "Dictionary-based compressive Fourier ptychography," Opt. Lett. **47**(9), 2314–2317 (2022).
42. A. Paszke, S. Gross, S. Chintala, *et al.*, "Automatic differentiation in pytorch," in *31st Conference on Neural Information Processing Systems (NIPS 2017)*, (2017).
43. D. P. Kingma and J. Ba, "Adam: A method for stochastic optimization," arXiv (2014).

44. P. C. Konda, L. Loetgering, K. C. Zhou, *et al.*, "Fourier ptychography: current applications and future promises," Opt. Express **28**(7), 9603–9630 (2020).
45. A. Ren, D. Lu, E. Wong, *et al.*, "Real-time observation of dynamic structure of liquid-vapor interface at nanometer resolution in electron irradiated sodium chloride crystals," Sci. Rep. **10**(1), 8596 (2020).
46. B. Chang, D. Li, Y. Ren, *et al.*, "A phosphorescent probe for in vivo imaging in the second near-infrared window," Nat. Biomed. Eng. **6**(1), 1–11 (2022).
47. L. Gu, D. J. Hall, Z. Qin, *et al.*, "In vivo time-gated fluorescence imaging with biodegradable luminescent porous silicon nanoparticles," Nat. Commun. **4**(1), 2326 (2013).
48. F. de Schaetzen, M. Fan, U. Alcolombri, *et al.*, "Random encounters and amoeba locomotion drive the predation of listeria monocytogenes by acanthamoeba castellanii," Proc. Natl. Acad. Sci. U. S. A. **119**(32), e2122659119 (2022).
49. Q. Huang, M. A. Cohen, F. C. Alsina, *et al.*, "Intravital imaging of mouse embryos," Science **368**(6487), 181–186 (2020).
50. M. Gómez-González, E. Latorre, M. Arroyo, *et al.*, "Measuring mechanical stress in living tissues," Nat. Rev. Phys. **2**(6), 300–317 (2020).
51. R. Cao, N. Divekar, J. Nuñez, *et al.*, "Neural space–time model for dynamic multi-shot imaging," Nat. Methods **21**(12), 2336–2341 (2024).
52. J. Sankaran, H. Balasubramanian, W. H. Tang, *et al.*, "Simultaneous spatiotemporal super-resolution and multi-parametric fluorescence microscopy," Nat. Commun. **12**(1), 1748 (2021).
53. S. Shin, D. Kim, K. Kim, *et al.*, "Super-resolution three-dimensional fluorescence and optical diffraction tomography of live cells using structured illumination generated by a digital micromirror device," Sci. Rep. **8**(1), 9183 (2018).
54. J. Kim and S. Chowdhury, "Space-time inverse-scattering of translation-based motion," Optica **12**(5), 643–653 (2025).
55. H. Luo, H. Chen, J. Xu, *et al.*, "Dynamic multiplexed intensity diffraction tomography using a spatiotemporal regularization-driven disorder-invariant multilayer perceptron," Opt. Express **32**(22), 39117–39133 (2024).